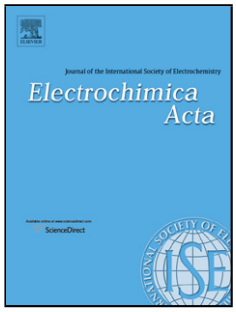

Title: Electrochemically modified boron-doped diamond electrode with Pd and Pd-Sn nanoparticles for ethanol electrooxidation

Authors: Christos K. Mavrokefalos, Maksudul Hasan, Worawut Khunsin, Michael Schmidt, Stefan A. Maier, James F. Rohan, Richard G. Compton, John S. Foord

PII: S0013-4686(17)31011-3
DOI: http://dx.doi.org/doi:10.1016/j.electacta.2017.05.039
Reference: EA 29474

To appear in: *Electrochimica Acta*

Received date: 18-1-2017
Revised date: 6-4-2017
Accepted date: 7-5-2017

Please cite this article as: Christos K.Mavrokefalos, Maksudul Hasan, Worawut Khunsin, Michael Schmidt, Stefan A.Maier, James F.Rohan, Richard G.Compton, John S.Foord, Electrochemically modified boron-doped diamond electrode with Pd and Pd-Sn nanoparticles for ethanol electrooxidation, Electrochimica Actahttp://dx.doi.org/10.1016/j.electacta.2017.05.039

Electrochemically modified boron-doped diamond electrode with Pd and Pd-Sn nanoparticles for ethanol electrooxidation

Christos K. Mavrokefalos[1], Maksudul Hasan*[1,2], Worawut Khunsin[3], Michael Schmidt[2], Stefan A. Maier[3], James F. Rohan[2], Richard G. Compton[4], John S. Foord*[1]

[1]Department of Chemistry, Chemistry Research Laboratory, University of Oxford, Mansfield Road, Oxford, OX1 3TA, England, UK

[2]Tyndall National Institute, University College Cork, Lee Maltings, Cork, Ireland

[3]Department of Physics, The Blackett Laboratory, Imperial College London, London, SW7 2AZ, England, UK

[4]Department of Chemistry, Physical and Theoretical Chemistry Laboratory, University of Oxford, South Parks Road, Oxford, OX1 3QZ, England, UK

*Corresponding author's e-mail: maksudul.hasan@chem.ox.ac.uk; john.foord@chem.ox.ac.uk; Phone: +44 01865 275967 - 275630 Fax: +44 01865 275410

Graphical Abstract

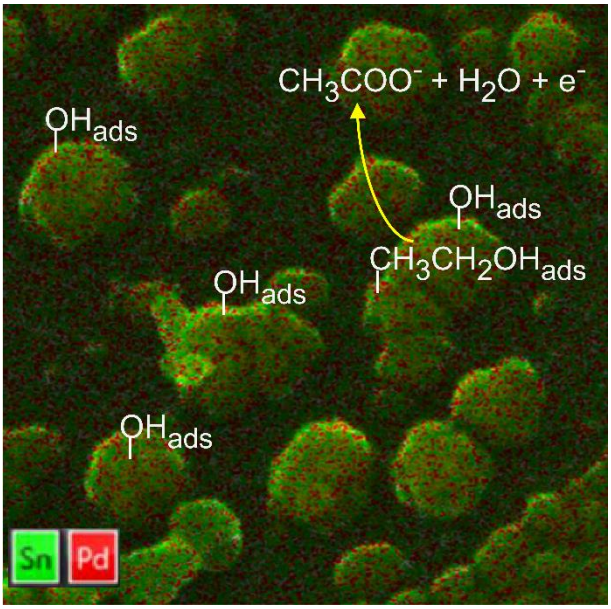

Highlights

- Hydrogen terminated boron doped diamond (HBDD) is reported as catalyst support.
- Electrochemical modification of HBDD with palladium-tin nanoparticles is described.
- Synergy between Sn and Pd enhances ethanol electrooxidation and poisoning effects.

Abstract: The modification of hydrogen terminated boron-doped diamond (HBDD) electrode with pure palladium (Pd) and Pd-Sn (tin) nanoparticles is described in this study. For synthesis of Sn/HBDD and Pd-Sn/HBDD electrode, a potentiostatic two-step electrochemical method involving the electrodeposition of Sn followed by Pd was used, respectively. The modification of the HBDD electrode with Sn and noble metal Pd by forming bimetallic Pd-Sn nanoparticle leads to a higher electrocatalytic activity. The electrocatalytic activity of the bimetallic Pd-Sn nanoparticles was evaluated towards the electrooxidation of ethanol in alkaline media and compared with that of the Pd nanoparticles alone. The bimetallic Pd-Sn nanoparticles modified HBDD electrode exhibits higher current densities and less poisoning effects during ethanol electrooxidation compared to Pd/HBDD. The proper tuning of the Pd loading on a foreign metal along with the surface termination effects of the BDD electrode plays a crucial role in achieving a high mass (4.26 x 10^6 mA/g) and specific (12.37 mA/cm^2) electrocatalytic activity of Pd towards ethanol electrooxidation. The aforementioned catalysts of this research possess a high poisoning resistance (I_f/I_b = 1.63) and stability towards ethanol electrooxidation in alkaline media.

Keywords: Diamond; Ethanol; Palladium; Tin; Nanoparticles.

1. Introduction

Metal nanoparticle surface modification of carbon substrates constitute common catalysts and have a plethora of benefits [1-5]. Of note are the increase of the oxidation efficiency of compounds in alkaline electrolytes compared to the non-functionalised catalyst, the oxidative removal of some poisons and consequently more tolerance as well as the durability of electrocatalyst. Boron-doped diamond (BDD) exhibits unique electrochemical properties in comparison with other carbon materials including low background current, high mechanical and electrochemical stability. Aside from that, resistance to fouling and corrosion in a hostile environment are also notable. Furthermore, it has a relatively low production cost when grown by chemical vapour deposition (CVD) [6-14]. All the aforementioned properties suggest this material as a promising substrate as a catalyst support. Moreover, the modification of diamond electrodes through the deposition of metal nanoparticles and/or metal oxides [10] as well as metal thin films [15] facilitates the sensitivity towards analytes which cannot be detected on the unmodified surface [16]. In addition, the latter can enhance the selectivity for various electroanalytical applications [17-19]. BDD electrodes modified with electrocatalytic metal nanoparticles have been established widely for their electrochemical

applications [6,14,20-26] and increased surface area in the field of adsorptive voltammetry [16,19,27]. An interesting feature of the diamond electrodes is the stable chemical terminations, which can be altered from oxygen to hydrogen by reacting the electrodes under a microwave plasma of hydrogen [28,31]. As a result, the hydrogen terminated BDD surface provides improved electrochemical response and physical stability [19]. It has been proved that a high concentration of hydrogen functionalities at the surface increases the electrical conductivity of BDD [32].

Diamond as a substrate has become attractive in fuel cell applications on account of its resistance to electrocorrosion [14,33,34]. Despite the fact that platinum (Pt) is one of the most active electrocatalyst anodes, it tends to be poisoned by the intermediates of ethanol species such as carbon monoxide (CO) [35]. Consequently, Pd is being investigated as an alternative catalyst, being more plentiful [36] than Pt and showing more tolerance to carbon monoxide [37] and promising as an efficient anode in the field of alkaline fuel cells [36,38,39]. Pd can also be utilised in numerous electrochemical applications including pharmaceutical applications [40], organic synthesis [41,42], sensing [43] and hydrogen storage [44,45].

The addition of foreign metals to a noble metal has become a potential approach of tailoring the catalytic properties in order to improve the poison tolerance and the ability of C-C bond cleavage [46]. The improved electrocatalytic performance of bimetallic catalysts is usually credited to the bifunctional mechanism and to the change of the electronic properties of the noble metal due to overlap of the electronic orbitals. In this work, Pd and Pd-Sn modified hydrogen terminated BDD electrodes have been studied for ethanol oxidation of relevance to the direct alkaline fuel cells (DAFC). The foreign metal changes the electronic structure of the noble metal that consequently alters its adsorption and selectivity towards the species e.g., Sn in the presence of Pt facilitates the dissociative adsorption of the ethanol species [47].

Herein, we report the electrochemical modification and surface pre-treatment of BDD electrode with Pd and bimetallic Pd-Sn nanoparticles. The bimetallic catalyst preparation involves a potentiostatic two-step electrochemical route with electrodeposition of Sn followed by Pd. The electrocatalytic activity of the bimetallic Pd-Sn nanoparticles was evaluated towards the electrooxidation of ethanol in alkaline media and compared with that of the Pd nanoparticles alone. The bimetallic Pd-Sn nanoparticles modified HBDD electrode exhibits higher current densities and less poisoning effects during ethanol electrooxidation compared to Pd/HBDD. In order to understand the correlation between the morphological, particle dispersion and electrocatalytic activities of Pd-Sn nanoparticles they were characterised by high resolution scanning electron microscopy (SEM) and X-ray photoelectron spectroscopy (XPS).

2. Experimental section

2.1 Chemical reagents

Chemical reagents Palladium (II) chloride ($PdCl_2$) and hydrochloric acid (HCl) were purchased from Sigma-Aldrich and used as received without any further purification.. Tin (II) methanesulfonate 50% aqua solution ($C_2H_6O_6S_2Sn$), methanesulfonic acid 70% aqua solution (CH_3SO_3H) were purchased from Alfa Aesar. All aqueous solutions were freshly prepared, using milli-Q water (>18 MΩ cm). All the solutions were deaerated using oxygen-free nitrogen gas for a minimum of 20 minutes prior to experiments.

2.2 Equipment and experimental set-up

BDD wafers ([B]>10^{21} cm^{-3}) of 10 x 10 x 0.6 mm were obtained from Element Six Co. (UK) and mounted in a home-built PTFE holder with a circular area of 0.38 cm^2 exposed to the electrolyte. The electrochemical measurements were performed with an Autolab PGSTAT 128N potentiostat/galvanostat. Electrochemical deposition was conducted at room temperature (24 ± 1.0°C) using a standard three electrode cell with a Pt counter electrode and Ag/AgCl reference electrodes. The electrochemical measurements were carried out at room temperature using a three electrode cell with a Pt and Hg/HgO (1 M KOH) as the counter and reference electrode, respectively. The electrochemical test data were analysied with OriginPro 8.5 software (OriginLab Ltd.). The morphology of the deposits was characterised by a FEI Helios Nanolab 600i field emission scanning electron microscope with an attached Oxford Instruments AZtech X-Max-80 energy dispersive X-ray spectroscopy unit for elemental mapping. All the images were taken with an acceleration voltage of 20 kV and a working distance (WD) of around 4 mm. The composition of the deposits was measured by XPS using an Al Kα (1486.6 eV) X-ray source and data were curve fitted using CasaXPS software [48] using a Shirley background [49]. The C 1s peak was calibrated to 285 eV with the following relative sensitivity factors: C 1s (1.0), O 1s (2.93), Pd 3d (16.0) and Sn 3d (25.1).

2.3 Modification of BDD electrodes

Prior to deposition, all BDD electrodes were put in MW-CVD at 600 °C, 45 Torr pressure, 1.5 kW microwave power and H_2 gas flow at 200 sccm for a duration of 45 minutes. At the end of 45 minutes, hydrogen plasma etching was achieved and the samples were cooled down in the MW-CVD chamber by switching off the heating and gradually reducing the microwave power until the plasma disappeared. The samples were cooled down naturally to room temperature. The electrodes were taken out from MW-CVD and examined for hydrogen termination by XPS. The O 1s/C 1s ratio within the XPS sampling depth is estimated at around 3%, which is 4 times less than that of an oxidised BDD surface [19].

Pd catalyst was then electrodeposited as nanoparticles onto HBDD from a deaerated 0.1M HCl solution containing 1mM $PdCl_2$ by a potentiostatic method. The deposition potential was held at -0.15V (vs Ag/AgCl) until 2.6, 5.2 and 10.4 mC/cm^2 charge passed through the surface. The corresponding metal loading of the aforementioned charges was 1.45, 2.90 and 5.80 μg/cm^2 respectively. The electrodepositions potential was chosen after cyclic voltammetry on bare diamond wafer in the same solution over the potential range (-0.1V to -0.4V) in which Pd reduction is occurred [50].

The second electrode comprised Pd-Sn/HBDD with Sn being electrodeposited onto HBDD from a deaerated 0.26M $C_2H_6O_6S_2Sn$ in 1M CH_3SO_3H solution through linear sweep voltammetry (LSV) at a potential between -0.6V and +0.0V (vs Ag/AgCl) at 0.01V/s for one cycle. Coulombic charge of Sn electrodeposition within this potential region of the LSV was calculated to be 158 mC/cm^2 i.e., 97 μg/cm^2. The Sn/HBDD electrode then was removed, rinsed with ultrapure water and dried with N_2. Pd nanoparticles were electrodeposited onto Sn/HBDD from a deaerated 0.1M HCl aqueous solution containing 1mM $PdCl_2$. Again, a potentiostatic method was used in which the potential was held at -0.15V (vs Ag/AgCl) until 2.6, 5.2 and 10.4 mC/cm^2 Coulombic charges passed through the electrode surface giving 1.45, 2.90 and 5.80 μg/cm^2 palladium loading.

3. Results and Discussions

3.1 Morphology and XPS characterisation of the deposits on HBDD

SEM images of Sn and Pd-Sn after the passage of 158 mC/cm^2 and 5.2 mC/cm^2 deposition charge for Sn and Pd, respectively, are shown in Figs. 1a-b. Sn nanoparticles in a non-uniform manner are displayed in Fig. 1a. The non-uniform nature of the deposit comes from the lateral conductivity of the diamond as well as of the non-uniform distribution of the B dopant as described in a previous report [51]. The non-uniform distribution of B dopant originated from the fact that B atoms are not all incorporated into the diamond lattice but are partly accumulated with C sp^2 impurities at the crystallite boundaries of diamond. According to the literature, a maximum value of B atoms is 10^{20} cm^{-3} but our BDD contains 10^{21} cm^{-3} due to the adaptation of new CVD method of using the gas mixture of B precursor, which gives a metallic-like conductivity [52]. Elemental mapping provides information for the deposition pattern of the Pd on Sn nanoparticles (Fig. 1b). As it can be seen from the Fig. 1b that Pd nanoparticles are deposited on Sn nanoparticles and another finding, which is obvious from the elemental mapping investigation is that Sn nanoparticles were preferentially deposited on the electroactive areas of diamond substrate whereas Pd nanoparticles deposited on Sn nanoparticles as well as on BDD surface. In other words, the conductive site of the underlying diamond and the active sites of Sn nanoparticles act as reactive centres for the deposition of Pd nanoparticles. It is of major importance to point out that the conductivity of diamond depends on the B dopant concentration. It

seems from the elemental mapping that Pd nanoparticles can be deposited on areas with lower B concentration whilst Sn is less likely to be deposited on such areas.

XPS was performed in order to investigate the elemental composition of Sn, Pd and Pd-Sn at the diamond interface for the samples in Fig. 2. Fig. 2a shows the survey scans of the Sn, Pd and Pd-Sn modified HBDDs, respectively. The wide range scans indicate that these electrodes contain C, O and the photoelectron peaks of the metal peaks. Pd has Pd $3d_{5/2}$ and Pd $3d_{3/2}$ peaks at 337.6 and 343 eV, respectively [53]. The Pd-Sn modified HBDD showed a small negative shift as seen in Fig. 2b where the Pd $3d_{5/2}$ and Pd $3d_{3/2}$ peaks were shifted to 336.9 and 342.2 eV, respectively, which implies some electronic interaction between the 3d orbitals of two metals which results in this binding energy shift. The negative binding energy shift (~ 0. 7 eV) of Pd $3d_{3/2}$ and Pd $3d_{5/2}$ can be attributed to the increase in interfacial charge of Pd atoms relative to the bulk material, and charge transfer that occurred from Sn atoms into the Pd contact layer, which increased the electron cloud densities of Pd atoms.

3.2 Voltammetric Characterisation

3.2.1 Electrodeposition of the electrocatalysts

A typical cyclic voltammogram of bare HBDD in a solution containing 0.26M $C_2H_6O_6S_2Sn$ in 1M CH_3SO_3H is shown in Fig. 3a. The Sn is deposited on the cathodic scan in the potential range of -0.49V and - 0.6V and stripped out in the anodic scan with a sharp peak at a potential of -0.35V. A pronounced nucleation loop in the cathodic scan indicates that Sn deposition on HBDD surface occurred through the formation of small nuclei followed by further growth. Linear sweep voltammetry technique was then applied within the potential region of 0.0V and -0.6V for the deposition of Sn as shown in the inset of Fig. 3a. A typical voltammogram of bare HBDD in a solution containing 1mM $PdCl_2$/0.1M HCl is also illustrated in Fig. 3b. The Pd is deposited in the forward scan in the potential range of 0.22V and -0.37V. The cathodic current peaked initially at 0.15V (peak C_1) and ramained steady until a sufficient overpotential was reached at -0.25V and then increased sharply to a maximum at -0.33V (peak C_3) near the diffusion limited reduction of Pd ions. The cathodic peak C_2 represents the adsorption of underpotentially deposited hydrogen on the electrodeposited Pd surface before the diffusion limited reduction of Pd ions occurs at peak C_3. Beyond this peak the current decreased as the mass transfer became diffusion dominant, reaching a minimum at -0.34V (peak C_4) followed by an increase due to bulk H_2 evolution (peak C_5). The potential region of 0.22-0.15V represents the Pd metal deposition without hydrogen underpotential deposition (H_{UPD}), and after this point i.e., in the cathodic range between -0.15V and -0.37V deposition occurs simultaneously with H_{UPD} onto the freshly deposited Pd , in which peaks A_2, A_4, A_5) are due to the H desorption process. The A_1/C_1 peaks show the Pd stripping from the electrode surface having a peak maximum at 0.58V and the reduction

peak at 0.14V in the anodic and cathodic scan, respectively. Pd was then deposited on the Sn surface of HBDD electrode by potentiostatic chronoamperometry method held at -0.15 V as shown in the inset of Fig. 3b.

3.2.2 Electrochemical activity of the electrocatalysts

The electrochemical activity of the electrocatalysts was characterised by cyclic voltammetry in 0.5M KOH. The behaviour of Pd nanoparticles (Pd loading is 5.80 μg/cm^2 on each electrode) on an oxygen terminated BDD (OBDD) surface and on a hydrogen terminated BDD (HBDD) surface was compared initially (Fig. 4a). In Fig. 4a, the following features are observed: (i) Pd oxidation and reduction peaks (A_1/C_1) at 0.03V and -0.23V, respectively; It can be attributed to the formation of a palladium oxide layer on the surface of the catalyst. However, the exact mechanism of the Pd oxidation remains unclear [54]. It has been generally accepted that OH^- ions are chemisorbed in the initial stage of the oxide formation and then are transformed into higher valence oxides at higher potentials [55-57]. (ii) Hydrogen adsorption occurred on the Pd surface in the cathodic scan at -0.7V and -0.9V (peaks C_2/C_3) and the corresponded desorption occurred in the anodic scan at -0.73V and -53V, respectively (peaks A_3/A_2). (iii) a prepeak (A'_1) appeared at -0.22V in the anodic scan before the main Pd surface oxidation process commenced, which corresponds to oxidation at favourable sites on the palladium surface [58]. The corresponding oxide reduction peak for A_1 may appear during limited potential scanning towards incomplete oxidation and reduction (peak A_1/C_1) of the Pd surface as described elsewhere [58]. However, the hydrogen terminated Pd/HBDD electrode showed higher current densities and the more ability to adsorb hydrogen ions than that of the oxygen terminated Pd/OBDD electrode. This is likely to arise from the fact that there is a high concentration of hydrogen functionalities on the surface and the conductivity is increased according to previous report [32]. Hence, our interest was focused on the hydrogen terminated BDD surfaces as electrode and modification of the electrode by electrochemically deposited shell-core Pd-Sn nanoparticles towards electrooxidation of ethanol. A proposed mechanism for the oxidation and reduction on the Pd catalyst in alkaline aqueous solution is described by the equations below. The peaks C_2, C_3 and A_3, A_2 that appear at the potential region -0.6V and -0.9V in the cathodic and anodic scan, respectively, are associated with the adsorption/absorption and oxidation of the hydrogen [54]:

$$Pd + H_2O + e^- \leftrightarrow Pd - H_{ads/abs} + OH^- \quad (1)$$

$$Pd - H_{ads/abs} + OH^- \leftrightarrow Pd + H_2O + e^- \quad (2)$$

The A_1 peak occurs at potentials of around 0.03V in the anodic scan is related to the adsorption of hydroxyl groups:

$$Pd + OH^- \leftrightarrow Pd - OH_{ads} + e^- \quad (3)$$

The chemisorbed OH^- ions are then transformed into higher-valence oxides at potentials between 0.1V and 0.5V in the anodic scan:

$$Pd - OH_{ads} + OH^- \leftrightarrow Pd - O + H_2O + e^- \quad (4)$$

$$Pd - OH_{ads} + Pd - OH_{ads} \leftrightarrow Pd - O + H_2O \quad (5)$$

A cathodic peak (C_1) at approximately -0.23V in the cathodic scan is associated with the reduction of Pd(II) oxide:

$$Pd - O + H_2O + 2e^- \leftrightarrow Pd + 2OH^- \quad (6)$$

The cyclic voltammogram of Sn/HBDD (Fig. 4b) does not show electrochemical activity in the potential range of -0.9V to 0.1V and thus, pure Sn is inactive within the electrochemical window where Pd is electrocatalytically active. However, a cathodic peak at potentials more negative than -1.1V and an anodic peak at -1.02V in the reverse scan are seen, which is due to deposition and dissolution of unknown electroactive species onto the Sn surface. The cyclic voltammograms of HBDD, Pd/HBDD and Pd-Sn/HBDD electrodes corresponding to 5.2 mC/cm^2 of Pd deposition charge (equivalent to 2.90 μg/cm^2) in alkaline aqueous solution are shown in Fig. 4c. Similar features to those observed for the Pd/OBDD and Pd/HBDD catalysts are distinguished over the same potential range. However, of note is the prepeak feature (A'_1) at -0.22V in the reverse (anodic) scan which only occurs at the Pd-Sn modified HBDD and is not seen at its Pd, bare HBDD or Sn modified counterparts [59-61] (see also Fig. 4b). Although a small prepeak (A'_1) of the Pd/HBDD is seen in Fig. 4a it is not detected in Fig. 4c for which the Pd loading was reduced by half. Therefore, the appearance of an intense prepeak (A'_1) in the Sn modified Pd-Sn/HBDD electrode in Fig. 4c with lower Pd content explains the synergy of the electronic interaction between two metals which resulted into a higher oxidation of the favorable sites of Pd-Sn bimetallic nanoparticles compared to that of Pd alone. The aforementioned features are consistent with the Sn nanoparticles serving as reactive centres for the subsequent deposition of Pd to forming a core-shell structure. The hydrogen functionalities increase the conductivity of the HBDD and reinforce the active sites for Sn deposition at the higher concentrated B dopant electrode surface, which in turn acts as reactive centres for the subsequent deposition of Pd nanoparticles. The modification of the HBBD electrode with transition metal Sn and noble metal Pd by forming bimetallic nanoparticles leads to higher currents and more hydrogen adsorption. Regarding the hydrogen evolution, more evidence is provided from the linear sweep voltammogram in Fig. 4d. The hydrogen evolution on the Pd-Sn/HBDD surface occurs on the cathodic scan at a potential of -1.0V, the onset

potential is much lower when Pd interacts with the underlying Sn compare to Pd/HBDD electrode alone in which hydrogen evolution occurs at -1.07V.

The metal coverage of Pd can be estimated from the charge obtained from the area under the voltammogram applying Faraday's Law. Determining the ratio of the charge required for desorption of an oxygen monolayer on the Pd (111) surface (0.424 mC cm^{-2}) [62] to that of Q_o which is the coulombic charge of the oxygen desorption on the Pd surface, the electroactive surface area (EAS) of the pure Pd electrocatalyst can be also estimated. In addition, the specific surface area (SSA) can be defined as the electroactive surface area divided by the metal loading. All the above information is included in Table 1.

3.3 Electrocatalytic performance of Pd-Sn nanoparticles on ethanol electrooxidation

The electrocatalytic activity of the Pd/HBDD and Pd-Sn/HBDD towards the oxidation of ethanol was evaluated in solutions containing 0.5M KOH and 1M EtOH and cyclic voltammograms were obtained. The results are shown in Figs. 5a-c. The onset potential for electrooxidation of ethanol is observed at -0.5V, which implies that the electrode is inactive before this overpotential. The current increases as the potential is scanned positively (anodic) of the onset electrooxidation potential and the peak current at around -0.1V, -0.12V and -0.02V were due to the ethanol oxidation on Pd/HBDD (1.45μg/cm^2), Pd-Sn/HBDD (2.90 μg/cm^2), and Pd-Sn/HBBD (5.80 μg/cm^2) electrodes, respectively, as shown in Fig. 5. However, the peak position is slightly shifted as the Pd loading increased, which is due to the electronic interaction of the Pd in the outer surface of the nanoparticles of metallic Sn. The peak in the forward scan refers to the oxidation of the fresh ethanol species accumulated on the surface. All electrodes are deactivated at the same potential around 0.1V and reactivated again in the reverse scan (cathodic) at -0.18V giving a second oxidation wave at around -0.24V [59,61]. The second peak implies the oxidation of the incomplete carbonaceous species of the ethanol. Previous studies suggested that the reduced current at more positive potentials was related to the formation of a Pd oxide layer on the surface of the electrode at higher potentials [55,63-65]. The formation of the oxide layer can block the adsorption of the reactive species onto the Pd surface and lead to a decrease in the electrocatalytic activity. As long as the positive going sweep proceeds more Pd oxide covers the surface of the electrode and therefore the current of the oxidation of ethanol is further decresaed [54]. The overall electrode resistance to poisoning by the incomplete oxidation of the adsorbed carbonaceous species (CH_3CO_{ads}) of the ethanol is correlated to the ratio of the forward oxidation current peak (I_f) and the backward oxidation current peak (I_b) [66,67]. In Fig. 5a, Pd-Sn modified HBDD with the lowest amount of Pd (2.6 mC/cm^2 charge i.e., 1.45 μg/cm^2,) gives a higher current responses by comparison with the Pd/HBBD electrode but the resistance to poisoning is relatively low (see also Table 1). The tolerance ratio towards the ethanol is improved when the amount of Pd is increased as

shown in Figs. 5b-c. Conversely, the Pd-Sn/HBDD with the higher Pd loading in Fig. 6b (2.90 μg/cm^2) not only showed higher current densities in comparison with Pd/HBDD itself but also the resistance of the electrode to poisoning by the absorbed ethanol species was higher. The tolerance ratio of the Pd-Sn/HBDD with 2.90 μg/cm^2 loading seems to have its highest value (I_f/I_b=1.63) at this specific loading. However, this value which is not only higher than the Pd/HBDD of the same metal loading (I_f/I_b=0.89) but also of the one which has the double the amount of palladium loading (I_f/I_b=1.35). Furthermore, there was a slight shift in the potential from -0.1V to -0.12V for the Pd modified HBDD and the Pd-Sn/HBDD, respectively. A proposed mechanism of the ethanol oxidation in alkaline aqueous solution at low-potential region (-0.9-0.4V) is described by the following equations [54]:

$$Pd + CH_3CH_2OH \leftrightarrow Pd-(CH_3CH_2OH)_{ads} \quad (7)$$

$$Pd-(CH_3CH_2OH)_{ads} + 3OH^- \leftrightarrow Pd-(CH_3CO)_{ads} + 3H_2O + e^- \quad (8)$$

The oxidation of the adsorbed acyl [$(CH_3CO)_{ads}$] intermediate by the adsorbed hydroxyl [$(OH)_{ads}$] occurs at potentials above -0.4V during the anodic scanning by cyclic voltammogram (Figs. 5a-c) as expressed by the following equations [54]:

$$Pd-(CH_3CO)_{ads} + Pd-OH_{ads} \leftrightarrow Pd-CH_3COOH + Pd \quad (9)$$

$$Pd-CH_3COOH + OH^- \leftrightarrow (CH_3COO^-)_{sol} + Pd + H_2O \quad (10)$$

On the other hand, when the loading of the catalyst was doubled the current responses of both Pd/HBDD and Pd-Sn/HBDD were almost the same (Fig. 5c). That means that the electronic interaction between the two metals decresaed as thicker overlayers of Pd nanoparticles formed on the initial Pd in more intimate contact with the Sn metal nanoparticles. Consequently, the threshold of Pd loading and therefore the better ratio of resistance to poisoning by the adsorbed ethanol species was 2.90 μg/cm^2 (5.2 mC/cm^2 passage of Pd deposition charge). Stability tests up to 1 hour and 40 minutes voltammetry in the ethanol solution showed good stability. Despite a small initial current drop during the first scans, Pd and Pd-Sn nanoparticles are bonded in a stable fashion on the hydrogen terminated surface.

Experiments were conducted also on Sn electrodes with 15 times more Pd on it and the result showed that there is no advantage for the interaction between the two metals. Clearly, a large over-layer of Pd was created on the surface of Sn nanoparticles and therefore, the current was increased but it was not higher than that of the Pd alone. In addition the tolerance towards the ethanol oxidation was reduced due to that of higher amount of Pd loading, hiding the electronic properties of the two metals as well as the properties and extra conductivity from the hydrogen termination. An overall

picture of the mechanism of ethanol electrooxidation reaction and at the same time the role of various amount of Pd loading towards the latter oxidation reaction is illustrated in Fig. 6.

3.4 Tafel analysis

The electrochemical activity of Pd and Pd-Sn modified HBDD electrodes was investigated further by measuring the anodic polarisation curve and calculating kinetic parameters from Tafel plots as shown in Fig. 7. The Tafel plots are calculated from the steady state cyclic voltammograms shown in Fig. 5. The quasi-steady-state cyclic voltammograms were achieved on Pd and Pd-Sn modified HBDD electrodes at a scan rates of 0.02 V/s after 20 cycles that was consistent with the recent work published by our group, in which HBDD or OBDD electrodes showed a good reversibility even at faster scan rates (0.02 to 0.1 V/s) [19]. In Fig. 7a, slopes in the lower onset potential region, namely charge transfer control region, are approximately the same for the both electrodes, which are 120 and 125 mV dec^{-1} for Pd/HBDD and Pd-Sn/HBDD, respectively, with the lower amount of Pd loading (1.45 $\mu g/cm^2$). The Tafel slope indicates that the kinetics of ethanol oxidation reaction in the lower potential region of -0.55V to -0.35V is dominated by the adsorption of hydroxyl ions on the Pd surface [54]. Nevertheless, the small deviation in the Tafel slope between the Pd/HBDD and Pd-Sn/HBDD shows that the kinetics of the ethanol oxidation reaction is not only controlled by the adsorption of hydroxyl by it also altered by other surface reactions e.g. oxide layer that is formed on the surface of the Pd as reported in section 3.2. The same description can be attributed for the Fig. 7b with 2.90 $\mu g/cm^2$ Pd loading catalysts. Each plot has been fitted to one linear region. The Tafel slope for Pd/HBDD (201 mV dec^{-1}) is higher than that of Pd-Sn/HBDD (126 mV dec^{-1}) in the potential region -0.55V to -0.35V indicating the adsorption of higher hydroxyl (OH_{ads}) ions on the surface of the shell-core Pd-Sn nanoparticles. The lowest value indicates the higher charge transfer during the ethanol electrooxidation on Pd-Sn/HBDD electrode compare to the counterpart Pd/HBDD. This is lileky due to the Sn core structure, which suppress the formation of the inactive oxide layer in the potential range higher than -0.35V. In Fig. 7c, the Tafel plot of the Pd/HBDD and Pd-Sn/HBDD with further increased Pd loading (5.80 $\mu g/cm^2$) is illustrated. The slopes differ slightly from each other in the charge transfer control region, which are 166 mV dec^{-1} and 152 mV dec^{-1} for the former and the latter, respectively. The Tafel slopes are similar for all electrodes and good agreement with the Temkin-type adsorption for hydroxyl (OH_{ads}) and acyl (CH_3CO_{ads}) ions at lower potential region (-0.55V to -0.35V) indicating the similarity of reaction mechanism for ethanol electrooxidation [54].

3.5 Amperometric response of the catalysts in ethanol

Chronoamperometry was performed to investigate the stability of Pd-Sn/HBDD electrocatalysts towards ethanol oxidation and the obtained result is compared with that of Pd/HBDD as demonstrated in Fig. 8. The electrodes were held at a fixed potential -0.15V and run for 7200 seconds. The current

density decayed sharply for the Pd/HBDD but is more gradual for the Pd-Sn/HBDD electrocatalyst. Current densities remain stable for much of this period and finally the results are consistent with the performance of the cyclic voltammetry as described in the previous section (section 3.3). To be more precise, the bimetallic Pd-Sn/HBDD showed the highest current response in relationship with the Pd/HBDD alone. The decreased current with the increase in time is attributed to the combined effects of electrocatalyst poisoning by the chemisorbed carbonaceous oxidative intermediates and the concentration polarisation with time (i.e., limited mass transport with increasing reaction time).

4. Conclusions

The hydrogen terminated boron doped diamond (HBDD) electrode was modified with Pd and Pd-Sn nanoparticles by an electrochemical technique. A potentiostatic electrochemical deposition method was used to deposit noble metal Pd and transition metal Sn as nanoparticles onto HBDD towards investigation of the electrocatalytic properties in ethanol oxidation. XPS and electrochemical experiments suggested that Pd deposited on the Sn surface. The scanning electron microscopic image and elemental mapping showed that Pd nanoparticles are deposited both on the surface of Sn nanoparticles and BDD substrate. The modification of the HBDD electrode with Sn and Pd by forming Pd-Sn nanoparticles leads to higher electrochemical activity. Ethanol oxidation on Pd-Sn/HBDD electrode surface occurs at higher current densities and with less electrode poisoning than Pd/HBDD alone. This phenomenon is attributed to the dispersion of the Sn nanoparticles on the HBDD electrode surface followed by the deposition of mono-dispersed Pd nanoparticles on their surface and consequently, electronic properties are altered in the metallic interfaces as well as in the reaction interfaces owing to electronic interaction between Pd and Sn nanoparticles. Hence, Pd loading is found to be the most important factor. Lower amounts of palladium form a thin over layer on top of the Sn nanoparticles and allows the electronic interaction between them while the higher amounts of Pd loading do not facilitate such interface interaction between the two metals. Finally, Pd-Sn/HBDD catalyst shows higher stability towards ethanol oxidation in comparison with the Pd/HBDD alone. The proper tuning of the Pd on a transition metal along with the surface termination effects of the boron doped diamond electrode plays a crucial role in achieving the high mass and specific electrocatlytic activity of Pd towards ethanol electrooxidation.

Acknowledgment

Authors acknowledge Marie Skłodowska Curie Actions co-funded Irish Research Council Elevate fellowship ELEVATEPD/2014/15.

Notes

The authors declare no competing financial interest.

References

[1] E. M. Cunha, J. Ribeiro, K. B. Kokoh, A. R. De Andrade, Preparation, characterisation and application of Pt-Ru-Sn/C trimetallic electrocatalysts for ethanol oxidation in direct fuel cell, Int. J. Hydrogen Energy 36 (2011) 11034–11042.

[2] R. S. Hsu, D. Higgins, Z. Chen, Tin-oxide-coated single-walled carbon nanotube bundles supporting platinum electrocatalysts for direct ethanol fuel cells, Nanotechnology 21 (2010) 165705.

[3] R. Loukrakpam, S. R. Brankovic, P. Strasser, A study of Au/C nanoparticles with Pt monolayer and sub-monolayer electrocatalysts for ethanol oxidation reaction, ECS Trans. 58 (2013) 1733–1736.

[4] E. M. Gacutan, M. I. Climaco, G. J. Telan, F. Malijan, H. Y. Hsu, J. Garcia, H. Fulo, B. J. Tongol, Nanostructured carbon-supported Pd electrocatalysts for ethanol oxidation: synthesis and characterisation, Adv. Nat. Sci. Nanosci. Nanotechnol. 3 (2012) 045016.

[5] V. Kepeniene, L. Tamasauskaite-Tamasiunaite, J. Jablonskiene, J. Vaiciuniene, R. Kondrotas, R. Juskenas, E. Norkus, Investigation of graphene supported platinum-cobalt nanocomposites as electrocatalysts for ethanol oxidation, J. Electrochem. Soc. 161 (2014) F1354–F1359.

[6] T. N. Rao, A. Fujishima, Recent advances in electrochemistry of diamond, Diam. Relat. Mater. 9 (2000) 384–389.

[7] G. M. Swain. Thin-Film Diamond II. Elsevier, San Diego.

[8] I. Shpilevaya, W. Smirnov, S. Hirsz, N. Yang, C. E. Nebel, J. S. Foord, Nanostructured diamond decorated with Pt particles: preparation and electrochemistry, RSC Adv., 4 (2014) 531.

[9] L. Chen, J. Hu, J. S. Foord, Electrodeposition of a Pt-PrO_{2-x} electrocatalyst on diamond electrodes for the oxidation of methanol, Phys. Status Solidi 209 (2012) 1792–1796.

[10] A. Kraft, Doped diamond: a compact review on a new, versatile electrode material, Int. J. Electrochem. Sci. 2 (2007) 355–385.

[11] X. Lu, J. Hu, J. S. Foord, Q. Wang, Electrochemical deposition of Pt-Ru on diamond electrodes for the electrooxidation of methanol, J. Electroanal. Chem. 654 (2011) 38–43.

[12] R. L. McCreery, Advanced carbon electrode materials for molecular electrochemistry, Chem.

Rev. 108 (2008) 2646–87.

[13] K. E. Toghill, R. G. Compton, Electrochemical non-enzymatic glucose sensors: a perspective and an evaluation, Int. J. Electrochem. Sci. 5 (2010) 1246–1301.

[14] R. G. Compton, J. S. Foord, F. Marken, Electroanalysis at diamond-like and doped diamond electrodes, Electroanalysis 15 (2003) 1349–1363.

[15] A. Chatterjee, J. S. Foord, Electrochemical deposition of nanocrystalline zinc oxide at conductive diamond electrodes, Diam. Relat. Mater. 15 (2006) 664–667.

[16] K. E. Toghill, R. G. Compton, Metal nanoparticle modified boron doped diamond electrodes for use in electroanalysis, Electroanalysis 22 (2010) 1947–1956.

[17] A. S. Lourenço, F. C. Sanches, R. R. Magalhães, D. J. E. Costa, W. F. Ribeiro, K. M. Bichinho, G. R. Salazar-Banda, M. C. U. Araujo, Electrochemical oxidation and electroanalytical determination of xyliot at a boron-doped diamond electrode, Talanta 119 (2014) 509–516.

[18] G. R. Mansano, A. P. P. Eisele, L. H. Dall'Antonia, S. Afonso, E. R. Sartori, Electroanalytical application of a boron-doped diamond electrode: improving the simultaneous voltammetric determination of amlodipine and valsartan in urine and combined dosage forms, J. Electroanal. Chem. 738 (2015) 188–194.

[19] I. Shpilevaya, J. S. Foord, Electrochemistry of methyl viologen and anthraquinonedisulfonate at diamond and diamond powder electrodes: the influence of surface chemistry, Electroanalysis 26 (2014) 2088–2099.

[20] M. Panizza, G. Cerisola, Application of diamond electrodes to electrochemical processes, Electrochim. Acta 51 (2005) 191–199.

[21] G. M. Swain, A. B. Anderson, J. C. Angus, Applications of diamond thin films in electrochemistry, MRS Bull. 23 (1998) 56-60.

[22] M. Wei, C. Terashima, M. Lv, A. Fujishima, Z. Z. Gu, Boron-soped diamond nanograss array for electrochemical sensors, ChemComm 24 (2009) 3624–6.

[23] M. Lv, M. Wei, F. Rong, C. Terashima, A. Fujishima, Z. Z. Gu, Electrochemical detection of catechol based on as-grown and nanograss array boron-doped diamond electrodes, Electroanalysis 22 (2010) 199–203.

[24] S. Szunerits, Y. Coffinier, E. Galopin, J. Brenner, R. Boukherroub, Preparation of boron-doped diamond nanowires and their application for sensitive electrochemical detection of

tryptophan, Electrochem. commun. 12 (2010) 438–441.

[25] D. Luo, L. Wu, J. Zhi, Fabrication of boron-doped diamond nanorod forest electrodes and their application in nonenzymatic amperometric glucose biosensing, ACS Nano 3 (2009) 2121–2128.

[26] M. Antonio, Q. Alfaro, S. Ferro, C. A. Martínez-Huitle, Y. M. Vong, Boron doped diamond electrode for the wastewater treatment, Chem. Soc. 17 (2006) 227–236.

[27] P. Gan, J. S. Foord, R. G. Compton, Ionic liquid-carbon nanotube modified screen-printed electrodes and their potential for adsorptive stripping voltammetry, Electroanalysis 44 (2014) 1886–1892.

[28] C. E. Nebel, N. Yang, H. Uetsuka, E. Osawa, N. Tokuda, O. Williams, Diamond nano-wires, a new approach towards, next generation electrochemical gene sensor platforms, Diam. Relat. Mater. 18 (2009) 910–917.

[29] H. Mehedi, C. Hebert, S. Ruffinatto, D. Eon, F. Omnes, E. Gheeraert, Formation of oriented nanostructures in diamond using metallic nanoparticles, Nanotechnology 23 (2012) 455302.

[30] A. Kriele, O. A. Williams, M. Wolfer, J. J. Hees, W. Smirnov, C. E. Nebel, Formation of nano-pores in nano-crystalline diamond films, Chem. Phys. Lett. 507 (2011) 253–259.

[31] W. Smirnov, J. J. Hees, D. Brink, W. Muller-Sebert, A. Kriele, O. A. Williams, C. E. Nebel, Anisotropic etching of diamond by molten Ni particles, Appl. Phys. Lett. 97 (2010) 17–20.

[32] C. E. Nebel, B. Rezek, D. Shin, H. Watanabe, Surface electronic properties of H-terminated diamond in contact with adsorbates and electrolytes, Phys. Status Solidi Appl. Mater. Sci. 203 (2006) 3273–3298.

[33] G. S. Oliveira, M. F. Stein, E. Saito, H. Zanin, L. S. Vieira, L. Raniero, V. J. Trava-Airoldi, A. O. Lobo, F. R. Marciano, Effect of gold oxide incorporation on electrochemical corrosion resistance of diamond-like carbon, Diam. Relat. Mater. 53 (2015) 40–44.

[34] B. C. Ramos, E. Saito E, V. J. Trava-Airoldi, A. O. Lobo, F. R. Marciano, Diamond-like carbon electrochemical corrosion resistance by addition of nanocrystalline diamond particles for biomedical application, Surf. Coatings Technol. 259 (2014) 732–736.

[35] F. C. Nart, T. Iwasita, On the adsorption of sulfate species on polycrystalline platinum, J. Electroanal. Chem. 308 (1991) 277–293.

[36] E. Antolini, Palladium in fuel cell catalysis, Energy Environ. Sci. 2 (2009) 915.

[37] L. Feng, X. Sun, C. Liu, W. Xing, Poisoning effect diminished on a novel PdHoOx/C catalyst for the electrooxidation of formic acid, Chem. Commun. 48 (2012) 419.

[38] E. Antolini, E. R. Gonzalez, Alkaline direct alcohol fuel cells, J. Power Sources 195 (2010) 3431–3450.

[39] M. Shao, Palladium-based electrocatalysts for hydrogen oxidation and oxygen reduction reactions, J. Power Sources 196 (2011) 2433–2444.

[40] E. R. Krishna, P. R. Muralidhar, M. Sarangapani, G. Hanmanthu, B. Geeta, K. R. Shoba, V. Ravinder, Synthesis of N_4 donor macrocyclic Schiff base ligands and their Ru (II), Pd (II), Pt (II) metal complexes for biological studies and catalytic oxidation of didanosine in pharmaceuticals, Spectrochim Acta - Part A Mol. Biomol. Spectrosc. 97 (2012) 189–196.

[41] J. Lu, H. Zhang, X. Chen, H. Liu, Y. Jiang, H. Fu, Palladium-catalyzed synthesis of aromatic ketones and isoindolobenzimidazoles via selective aromatic C-H bond acylation, Adv. Synth. Catal. 355 (2013) 529–536.

[42] X. F. Wu, H. Neumann, M. Beller, Palladium-catalyzed oxidative carbonylation reactions, ChemSusChem 6 (2013) 229–241.

[43] C. M. Chang, M. H. Hon, I. C. Leu, Outstanding H_2 sensing performance of Pd nanoparticle-decorated ZnO nanorod arrays and the temperature-dependent sensing mechanisms, ACS Appl. Mater. Interfaces. 5 (2013) 135–143.

[44] S. B. Kalidindi, H. Oh, M. Hirscher, D. Esken, C. Wiktor, S. Turner, G. Van Tendeloo, R. A. Fisher, Metal@COFs: covalent organic frameworks as templates for Pd nanoparticles and hydrogen storage properties of Pd@COF-102 hybrid material, Chem - A Eur. J. 18 (2012) 10848–10856.

[45] F. Ksar, G. K. Sharma, F. Audonnet, P. Beaunier, H. Remita, Palladium urchin-like nanostructures and their H_2 sorption properties, Nanotechnology 22 (2011) 305609.

[46] A. Brouzgou, S. Q. Song, P. Tsiakaras, Low and non-platinum electrocatalysts for PEMFCs: current status, challenges and prospects, Appl. Catal. B Environ. 127 (2012) 371-388.

[47] F. Colmati, E. Antolini, E. R. Gonzalez, Effect of temperature on the mechanism of ethanol oxidation on carbon supported Pt, PtRu and Pt_3Sn electrocatalysts, J. Power Sources 157 (2006) 98-103.

[48] www.casaxps.com.

[49] L. Ley, S. Kowalczyk, R. Pollak, D. A. Shirley, X-ray photoemission spectra of crystalline and

amorphous Si and Ge velence bands, Phys. Rev. Lett, 29 (1972) 1088–1092.

[50] L. X. Ding, A. L. Wang, Y. N. Ou, Q. Li, R. Guo, W. X. Zhao, Y. X. Tong, G. Ren-Li, Hierarchical Pd-Sn alloy nanosheet dendrites: an economical and highly active catalyst for ethanol electrooxidation, Sci. Rep. 3 (2013) 1181.

[51] C. K. Mavrokefalos, G. W. Nelson, C. G. Poll, R. G. Compton, J. S. Foord, Electrochemical aspects of Pt-Cu and Cu modified boron-doped diamond, Phys. Status Solidi Appl. Mater. Sci., 212 (2015) 2559-2567.

[52] K. E. Bennet, K. H. Lee, J. N. Kruchowski, S. Y. Chang, M. P. Marsh, A. A. Van Orsow, A. Paez, F. S. Manciu, Development of conductive boron-doped diamond electrode: a microscopic, spectroscopic, and voltammetric study, Materials 6 (2012) 5726-5741.

[53] C. D. Wagner, W. M. Riggs, L. E. Davis, J. F. Moulder, G. E. Muilenburg. Handbook of X-ray Photoelectron Spectroscopy, Minnesota, 1979.

[54] Z. X. Liang, T. S. Zhao, J. B. Xu, L. D. Zhu, Mechanism study of the ethanol oxidation reaction on palladium in alkaline media, Electrochim. Acta. 54 (2009) 2203–2208.

[55] M. Grdeń, A. Czerwiński, The study of electrochemical palladium behavior using the quartz crystal microbalance, J. Solid State Electrochem. 12 (2008) 375–385.

[56] L. Vračar, S. Burojević, N. Krstajić, The surface processes at Pd-Ni alloy in acid and alkaline solutions, Int. J. Hydrogen Energy 23 (1998) 1157–1164.

[56] C. M. Jeong, C.H. Pyun, I. H. Yeo, Voltammetric studies on the palladium oxides in alkaline media, J. Electrochem. Soc. 140 (1993) 1986.

[58] G. Denuault, C. Milhano, D. Pletcher, Mesoporous palldium-the surface electrochemistry of palladium in aqueous sodium hydroxide and the cathodic reduction of nitrite, Phys. Chem. Chem. Phys. **7** (2005) 3545–3551.

[59] J. Cai, Y. Zeng, Y. Guo, Copper@palladium-copper core-shell nanospheres as a highly effective electrocatalyst for ethanol electro-oxidation in alkaline media, J. Power Sources 270 (2014) 257–261.

[60] G. Z. Hu, F. Nitze, X. T. JiaSharifi, H. R. Barzegar, E. Gracia-Espino, T. Wagberg, Reduction free room temperature synthesis of a durable and efficient Pd/ordered mesoporous carbon composite electrocatalyst for alkaline direct alcohols fuel cell, RSC Adv. 4 (2014) 676–682.

[61] C. Peng, Y. Hu, M. Liu, Y. Zheng, Hollow raspberry-like PdAg alloy nanospheres: high

electrocatalytic activity for ethanol oxidation in alkaline media, J. Power Sources 278 (2015) 69–75.

[62] M. S. Ahmed, S. Jeon, Synthesis and electrocatalytic activity evaluation of nanoflower shaped Ni-Pd on alcohol oxidation reaction, J. Electrochem. Soc. 161 (2014) F1300–F1306.

[63] J. Bagchi, S. K. Bhattacharya, Electrocatalytic activity of binary Palladium Ruthenium anode catalyst on Ni-support for ethanol alkaline fuel cells, Transit Met. Chem. 32 (2007) 47–55.

[64] M. Grden, J. Kotowski, A. Czerwinski, The study of electrochemical palladium behavior using the quartz crystal microbalance, J. Solid State Electrochem. 4 (2000) 273–278.

[65] J. Prabhuram, R. Manoharan, Effects of incorporation of Cu and Ag in Pd on electrochemical oxidation of methanol in alkaline solution, J. Appl. Electrochem. 28 (1998) 935–941.

[66] M. Chen, Z. B. Wang, Y. Ding, G. P. Yin, Investigation of the Pt-Ni-Pb/C ternary alloy catalysts for methanol electrooxidation, Electrochem. commun. 10 (2008) 443–446.

[67] J. Knudsen, A. U. Nilekar, R. T. Vang, J. Schnadt, E. L. Kunkes, J. A. Dumesic, M. Mavrikakis, F. Besenbacher, A Cu/Pt near-surface alloy for water-gas shift catalysis, J. Am. Chem. Soc. 129 (2007) 6485-6490.

Figure Captions:

Fig. 1. SEM image of (a) Sn deposited on HBDD (158 mC /cm^2) through linear sweep voltammetry between the potentials of -0.6V and 0.0V at a sweep rate of 0.01 V/s and (b) elemental mapping of Pd-Sn on HBDD, in which Pd deposited (5.2 mC/cm^2) on Sn nanoparticles by a potentiostatic method at -0.15V.

Fig. 2. XPS spectra of (a) wide range scans of the Sn/HBDD, Pd/HBDD and Pd-Sn/HBDD, respectively and (b) typical Pd 3d peaks of the Pd and Pd-Sn modified HBDD catalysts.

Fig. 3. (a) Cyclic voltammogram of bare HBDD in a solution containing 0.26M $C_2H_6O_6S_2Sn$ in 1M CH_3SO_3H at scan rate of 0.01V/s (inset: linear sweep voltammogram of Sn deposition in 0.26M $C_2H_6O_6S_2Sn$ in 1M CH_3SO_3H on bare HBDD). (b) Cyclic voltammogram of bare HBDD in a solution containing 0.1M HCl and 1mM $PdCl_2$/0.1M HCl respectively at scan rate of 0.01 V/s (inset: chronoamperogram of Pd deposition in 1mM $PdCl_2$/0.1M HCl on bare HBDD at constant potential of -0.15V).

Fig. 4. Cyclic voltammogram of (a) Pd/OBDD and Pd/HBDD (5.80 µg/cm^2), (b) Sn/HBDD (97 µg/cm^2), (c) Pd and Pd-Sn modified HBDD (2.90 µg/cm^2), and (d) Linear sweep voltammograms of the Pd and Pd-Sn modified HBDD (2.90 µg/cm^2), respectively in 0.5M KOH solution at scan rate of 0.02 V/s (all CVs were started from open circuit potential).

Fig. 5. (a, b) Cyclic voltammograms of Pd and Pd-Sn modified HBDD with 1.45 µg/cm^2 (i.e., 2.6 mC/cm^2 charge) and 2.90 µg/cm^2 (i.e., 5.2 mC/cm^2 charge) Pd loading, respectively in 0.5M KOH and 1M EtOH at scan rate of 0.02 V/s. (c) Cyclic voltammograms of Pd and Pd-Sn modified HBDD (with 5.80 µg/cm^2: Pd loading) in 0.5M KOH and 1M EtOH at scan rate of 0.02 V/s. (All CVs were started from open circuit potential). Cyclic voltammograms shown here are steady state taken after 10 cycles.

Fig. 6. Fig. 6. (a) Pd-Sn atomic arrangement with mechanistic pathways of EtOH electrooxidation, in which Sn atoms donate electron cloud to the Pd interfacial contact layer thus facilitating the adsorption of the hydroxyl and ethanol species (b) representation of the Pd loadings of shell-core Pd-Sn nanostructures and their ability to enhance the ethanol oxidation reaction (EOR).

Fig. 7. Tafel plots of anodic polarisation curve for ethanol oxidation in 0.5M KOH and 1M EtOH: (a, b) of Pd and Pd-Sn modified HBDD with 1.45 µg/cm^2 (i.e., 2.6 mC/cm^2) and 2.90 µg/cm^2 (i.e., 5.2 mC/cm^2) Pd loading, respectively. (c) of Pd and Pd-Sn modified HBDD with 5.80 µg/cm^2 (i.e., 10.5 mC/cm^2) Pd loading.

Fig. 8. (a, b) Chronoamperometric response of Pd and Pd-Sn modified HBDD in 0.5M KOH and 1M EtOH at potential -0.15 V, in which Pd deposition charge corresponded to 2.6 mC/cm^2 and 5.2 mC/cm^2, respectively.

Figures:

Fig. 1.

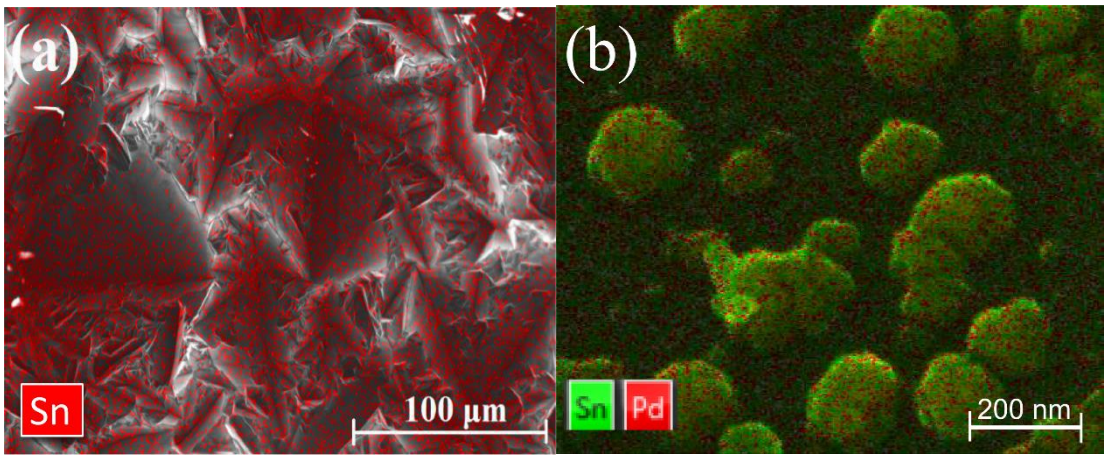

Fig. 2.

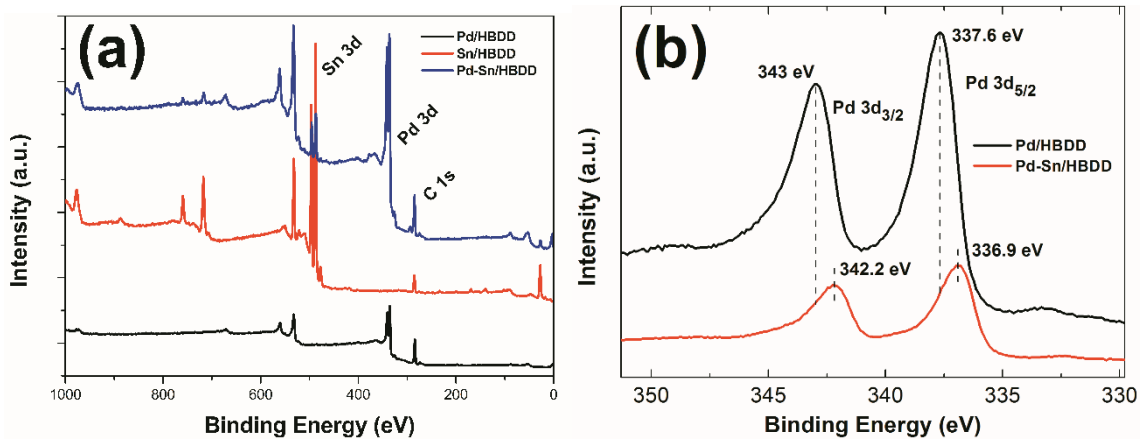

Fig. 3.

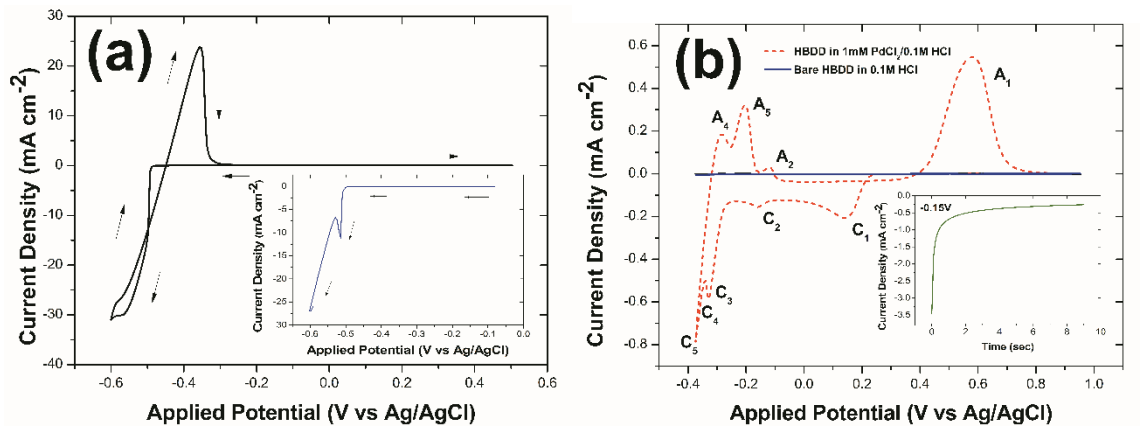

Fig. 4.

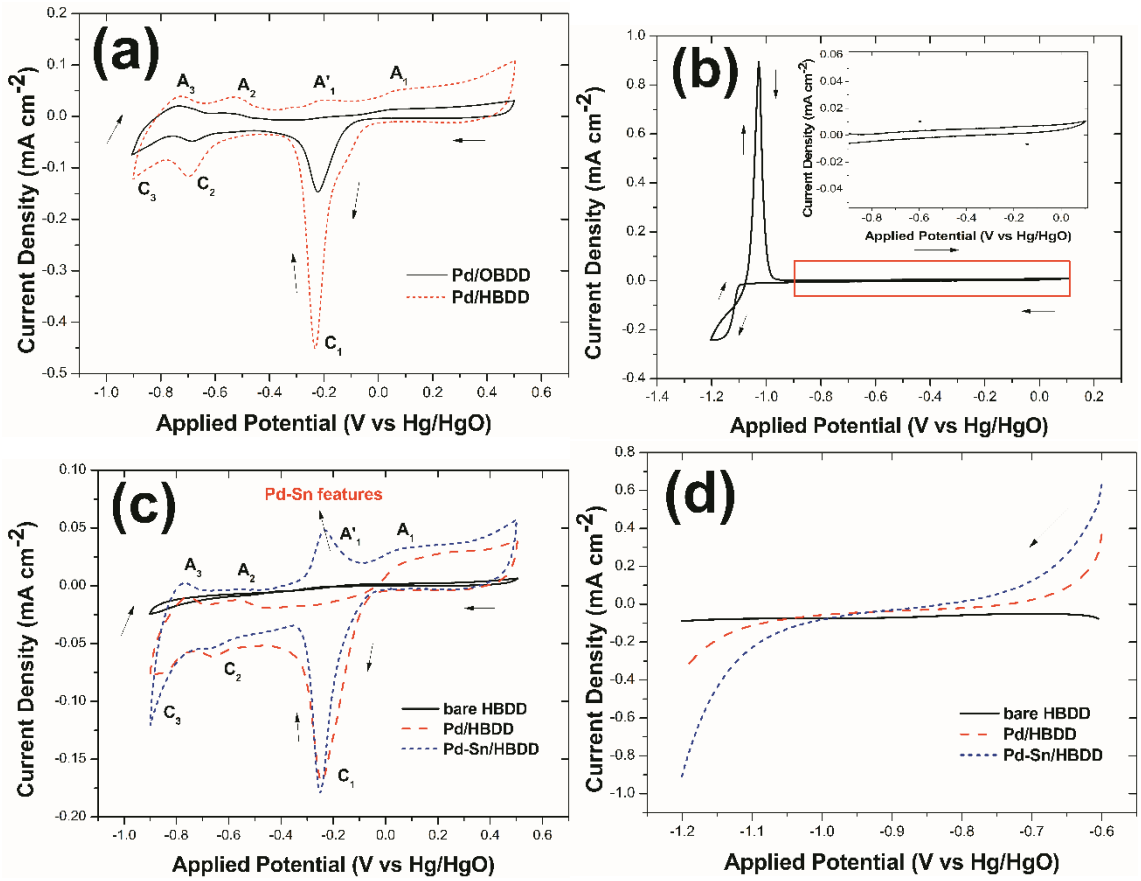

Fig. 5.

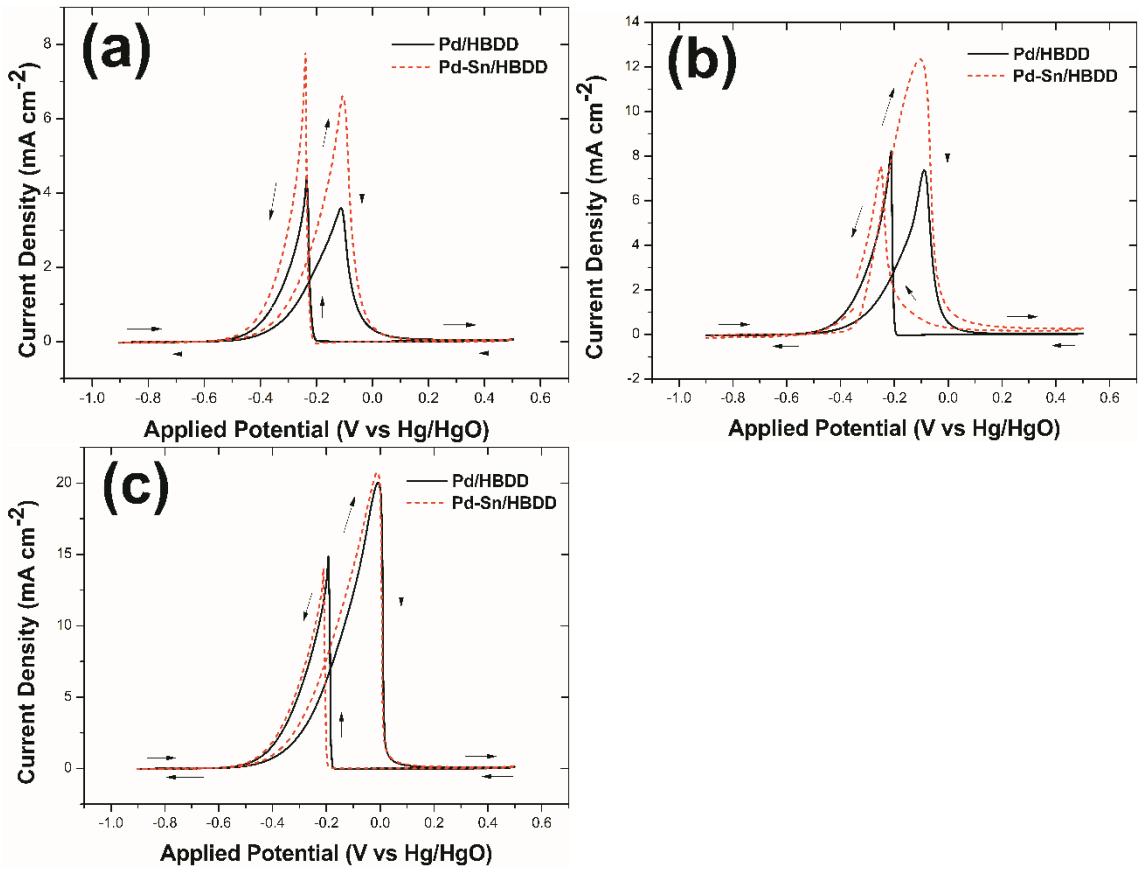

Fig.6.

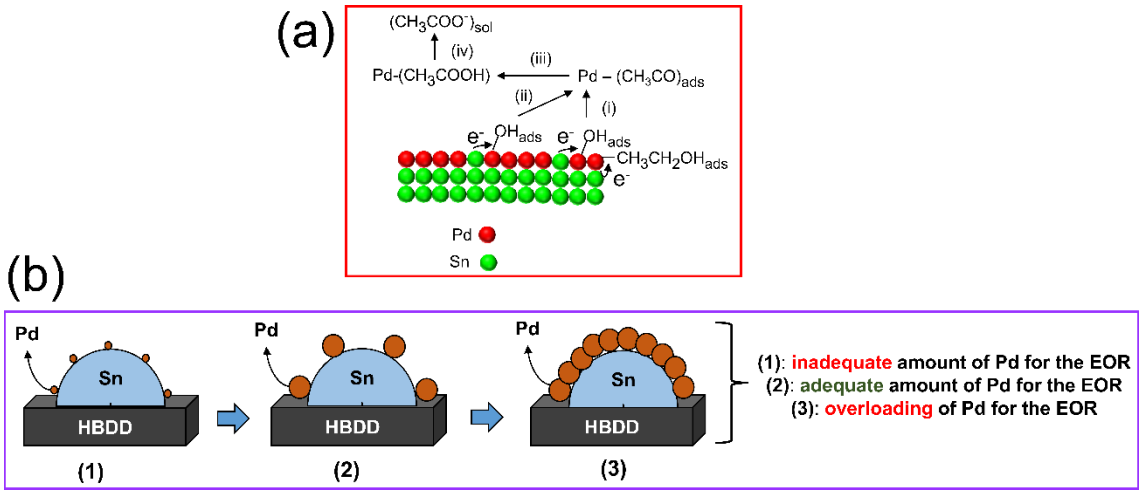

Fig.7.

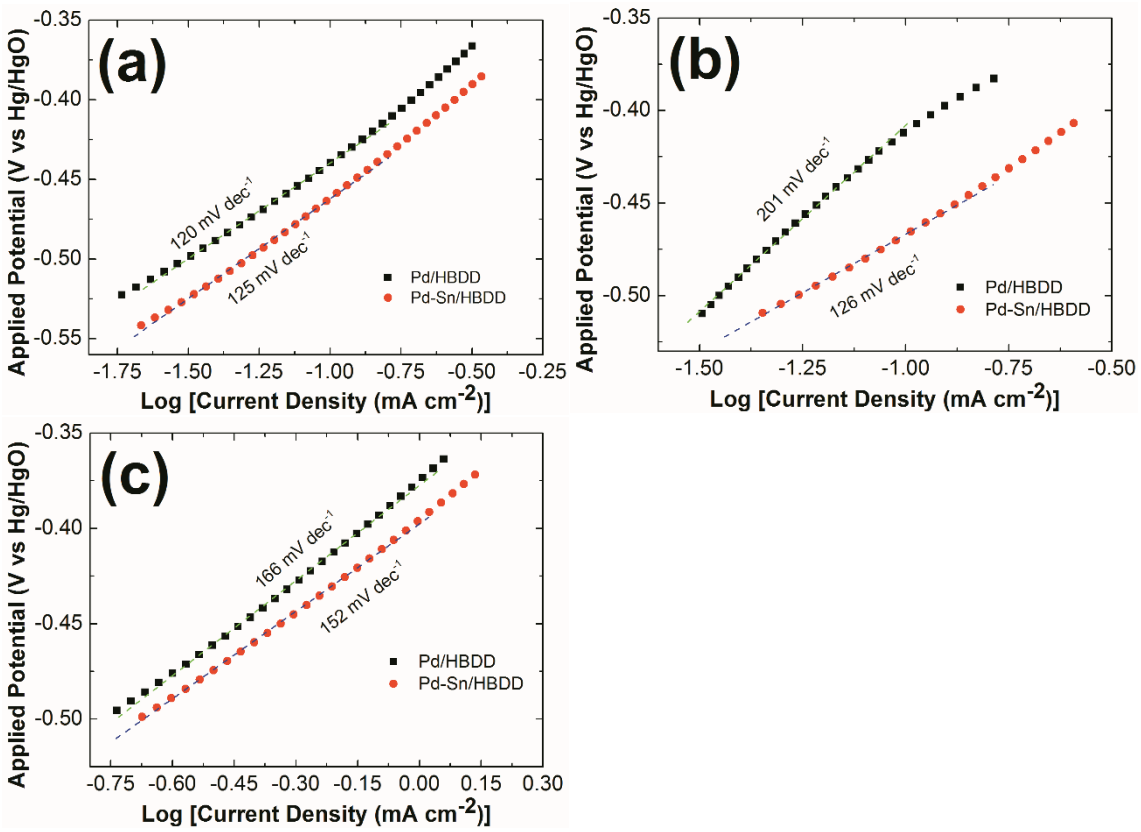

Fig. 8.

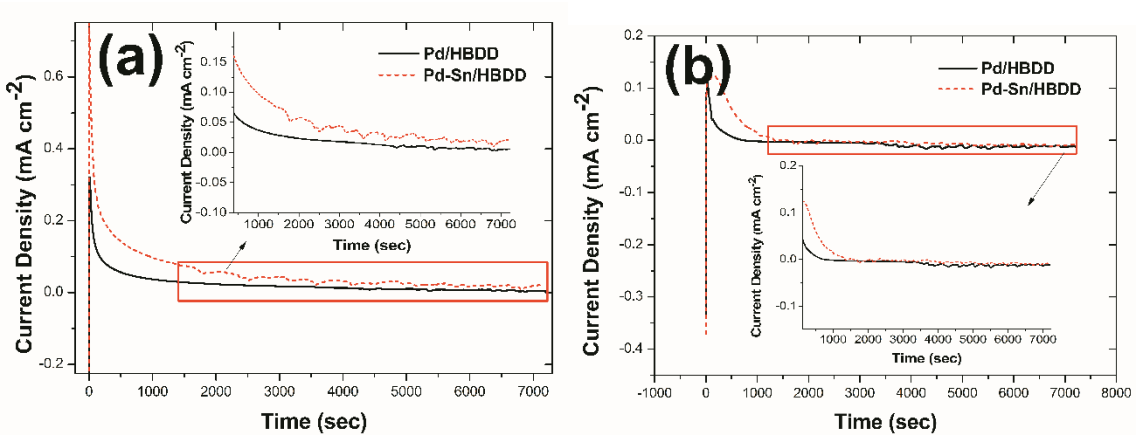

Table 1 Pd features after electrodeposition through chronoamperometry.

a/a	Electrodes	Charge (mC/cm^2)	Pd loading ($\mu g/cm^2$)	O des. charge (mC/cm^2)	Electroactive surface area, EAS (cm^2/cm^2)	Specific surface area, SSA (m^2/g)	Mass activity (mA/g) x 10^6	Particles size (nm)	Forward peak current (I_f), specific activity (mA/cm^2)	I_f/I_b
1	Pd/HBDD	2.6	1.45	0.71	1.67	115.17	2.48	4.33	3.60	0.81
	Pd-Sn/HBDD			0.81	1.92	132.41	4.56	3.77	6.61	0.86
2	Pd/HBDD	5.2	2.90	0.71	1.67	57.59	2.55	8.66	7.39	0.89
	Pd-Sn/HBDD			0.74	1.74	**60.00**	**4.26**	8.32	**12.37**	**1.63**
3	Pd/HBDD	10.5	5.8	1.81	4.28	73.79	3.45	6.76	20.02	1.35
	Pd-Sn/HBDD			1.66	3.91	67.41	3.58	7.40	20.78	1.49